Oral presentation | Aero-acoustics
Aero-acoustics-II
Mon. Jul 15, 2024 2:00 PM - 3:30 PM Room B

[2-B-01] Turbulent Boundary Layer Noise of Fighter Aircraft Canopy

*Muhammed Alperen Kuş[1], Baha Zafer[2] （1. Roketsan Inc., 2. Istanbul Technical University）

Keywords: CAA, Ffowcs Williams-Hawkings, Turbulent, Canopy

Twelfth International Conference on
Computational Fluid Dynamics (ICCFD12),
Kobe, Japan, July 14-19, 2024

Turbulent Boundary Layer Noise of Fighter Aircraft Canopy

M. A. Kuş*, B. Zafer**
Corresponding author: kus17@itu.edu.tr
* Roketsan Missle Inc, Turkey.
** Istanbul Technical University, Turkey.

Abstract: F-16 Fighting Falcon fighter aircraft developed by General Dynamics , which is in the Turkish Air Force (TAF) inventory, has been selected for the project. Real dimensions are used in the selected fighter aircraft canopy geometry, and it was simplified in detail and made suitable for creating a mesh structure. Unstructural mesh structure is applied on canopy geometry. Computations are performed at three different Mach values. These values are Mach 0.65, Mach 1.05, and Mach 1.45. Since aerodynamic and characteristic properties are different for each Mach value, calculations are made separately. As a result of these calculations, three different mesh types are created and the mesh structure suitable for each Mach value is used in the computations. Three different turbulent models are performed for each Mach value. These turbulent models are Wilcox k-ω, Shear Stress Transform (SST) k-ω Reynold Average Navier Stokes (RANS) models; and Detached-Eddy Simulation (DES) model. Unsteady numerical fluid flow results are used for aeroacoustic signals. Aeroacoustic results are obtained using the Ffowcs Williams-Hawkings (FW-H) and Fast-Fourier Transform (FFT) post processing methods. Then, the computation results obtained these two different post processing methods for the same points are compared.

Keywords: Canopy, Numerical Algorithms, Computational Fluid Dynamics, Turbulence Modeling, Aeroacoustics.

1 Introduction

The physics of aircraft noise production shows that acoustics is actually a sub-branch of aerodynamics. In addition to the thrust force of the aircraft, which is an aerodynamic force and is the main source of aircraft noise, the noise generation mechanism is closely connected with aerodynamic phenomena due to the aerodynamic noise generated in the boundary layer surrounding the moving aircraft [24].

The noise properties of civil and military aircraft operations are distinct. The difference in noise from a fighter aircraft and civil jet aircraft is easily heard. The operations of fighter aircrafts pose a significant noise problem. The turbulence generated in high-speed jet flows is responsible for the dominant noise associated with high-performance military engines. The jet engines that power the fighter aircraft are often operated at off design conditions; thus, producing shocks in the jet plume. The component of broadband shock associated noise is produced in addition to the turbulent mixing noise. Thus, jet noise can have multiple components [6, 23]. There are three situations with high noise impact: 1) Settlements or communities around land and naval bases where fighter aircraft; 2) Crew located near the fighter aircraft, which takeoff at maximum power; and, 3) Pilots inside the fighter aircraft canopy. The first situation pertains to noise in the far field, while the second and third represents noise in the near field [23].

The other source of noise is the aerodynamic noise generation in the boundary layer of the airplane as it moves through the air. The noise inside the cockpit and is high during the operation of a fighter aircraft. Turbulent boundary layer noise of fighter aircraft canopy is the second most important source for noise, which underlies the fuselage noise problem and distracts the pilot in fighter aircrafts. Even, in high speed fighter aircraft the aerodynamic noise may contribute 95 percent of the noise energy and might become the practical limiting factor rather than the engine noise. The frequency spectrum and energy of the boundary layer noise and general aerodynamic noise were affected by the sound transmission characteristics ofthe fuselage wall. The peak energy in the spectrum apparently shifts to higher frequencies as the velocity increases. They may go up to 150 dB but are easily attenuated by the fuselage wall. In the cockpit of certain fighter aircrafts sound pressure levels around 130 dB were recorded at an airspeed of 223.5 meter per second [24].

Pilots also carry on radio communication, which increases their noise exposure. The speech intelligibility of the radio communication is a significant safety parameter, and, in order for it to be improved, cockpit noise should be minimized and the noise attenuation of flight helmets and headsets maximized [18]. Turbulent boundary layer noise of fighter aircraft canopy is a subject that needs further research and study. The motivation for this study is to define the problems and bring materials sciences into the work, paving the way for low-noise aeroacoustic configuration designs for both the pilot and the fuselage. The result of this paper can be used to lower the noise levels or improve the sound insulation with minor geometrical changes and the use of different materials, and should lead up for a lot number of calculations that can be applied to designs in an industrial setting.

Acoustic noise prediction theories for turbulent sources of sound have demonstrated successful in the times past. However, their applications were mostly limited to elementary flow problems. Problems can be solved by current Computational Aeroacoustics (CAA) methods even for very complex geometries and it is possible to get good results by taking the impact of flow on propagation of sound into account. In addition, numerical approaches of Reynolds Average Navier Stokes (RANS) equations ensure average data to connected flows and efficient local knowledge in the matter of the surrounding non-uniform flow for many geometries. Therefore, RANS can assist in the extension of statistical sound source modeling beyond basic boundary layer flows to more sophisticated and general turbulent flow situations. The computational solution is based on a transient RANS model for solve the time-averaged turbulence case and a transient CAA method of the associated wide band noise case.

2 Problem Statement

In this study the RANS/Detached-Eddy Simulation (DES)/CAA methods are applied to make the turbulent boundary layer noise of the fighter aircraft canopy. The computations made with different turbulent models and post processing methods are compared to reach the optimum result for noise estimations. The gains made can be applied to the actual work on the General Dynamics F-16 Fighting Falcon aircraft that is chosen to be used. The noise in the turbulent boundary layer of the fighter aircraft canopy geometry is computed in three flow regimes (subsonic, transonic, supersonic), to help further studies for various noise situations.

Moreover, in this section, the canopy geometry in which the computations are made, the flight conditions required for the computations, and the mesh structure applied on the canopy geometry are explained.

2.1 Geometry

F-16 fighter aircraft developed by General Dynamics is selected to be used as as a result of literature review and numerical aerodynamics and aeroacoustics review. The Computer-Aided Design (CAD) file of the geometry was taken from the Istanbul Technical University (ITU) archive.

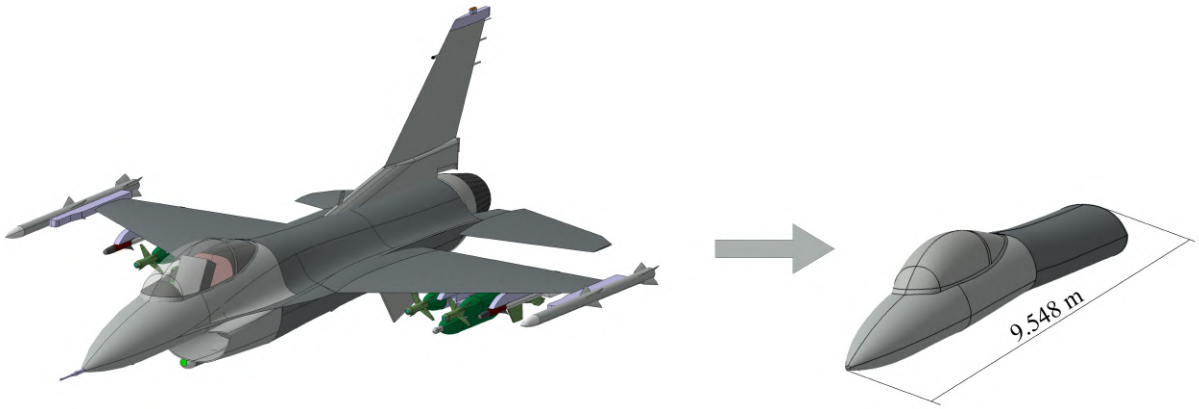

Figure 1: Full scale geometry of F-16 fighter aircraft and the canopy section used in the study

Some simplifications have been made to make the geometry of the F-16 fighter aircraft ready for computation. The wings, horizantal tail, vertical tail, bombs, pitot tube, Conformel Fuel Tank (CFT), engine and engine mounth are eliminated. Necessary corrections are made in the CATIA commercial

software. The geometry is used in full scale dimensions. Simplifications and final geometry are given in Figure 1.

2.2 Flight Conditions

The operational flight/ambient condition is the condition that makes up the longest portion of a fighter aircraft's mission envelope. Therefore, these conditions are mainly taken into account when creating the mesh. The operational flight/ambient conditions are calculated at NASA's "Air Viscosity Sutherland's Formula" webpage, given in Table 1.

Table 1: Properties of flight conditions

Flight Condition	Altitude [m]	Angle of Attack [°]	Atmosphere T_{static} [K]	Atmosphere P_{static} [Pa]	Air Density (ρ) [kg/m^3]	Dynamic Viscosity (μ) [Ns/m^2]	Speed of Sound [m/s]
Operational	12000	0	217	19391	0.31217	1.37701×10^{-5}	295.1

Flight conditions were determined to include three different flow regimes (subsonic, transonic, supersonic). When determining this scope, the following three situations were taken into account: 1) The turbulent boundary layer varies in different flow regimes; 2) Differences in pressures and pressure distributions occurring in different flow regimes; and, 3) Assisting further studies for various noise situations as mentioned above. Since there was no control surface command, different angle of attack and side slip angle in the analyses, the effects of flow regimes on the load, moment and difficulties encountered in terms of control were not taken into account.

2.3 Mesh

The mesh applied onto the geometry is created using the Pointwise commercial software. The important element in creating the mesh is to build the geometry with the minimum number of elements in order to make the computation within the least amount of time. In addition, in order to model the boundary layer velocity distribution in the most accurate way, the boundary layer mesh is placed on the geometry with the "T-Rex" option enabled in Pointwise.

The boundary layer is the region where the velocity gradient is very high and the viscosity effects are dominant. This region must be subdivided into much smaller elements than the rest of the geometry. Since the flow is completely turbulent, the goal in the boundary layer network structure is to reduce the element size to the smallest eddy size. The boundary layer mesh structure is modeled with the first layer thickness and a growth coefficient with layers stacked on top of each other.

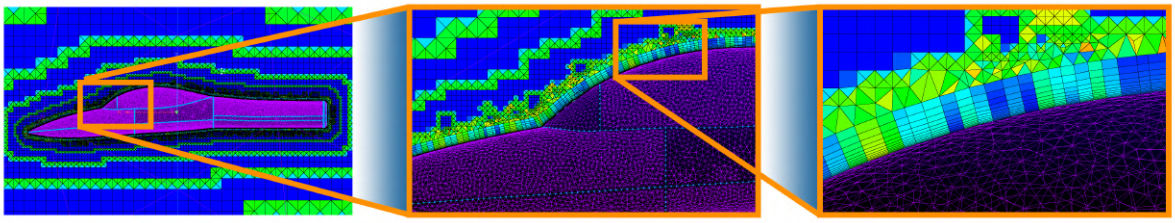

Figure 2: Boundary layer mesh structure near canopy section within detail

When calculating the boundary layer, the y^+ value is used to find the thickness of the first layer. This value is expected to be $y^+ \leq 1$, although there are different upper limits in the literature. The most accepted value for viscous substrates is $y^+ < 5$. However, in this project, the value of y^+ is taken as 200 to keep the mesh face count lower and avoid computational overload. The boundary layer mesh structure is given Figure 2. The following equations are used to calculate the boundary layer thickness and the length of first cell.

$$C_f = \frac{0.074}{Re^{1/5}}, \tau_{wall} = \frac{C_f \rho U^2}{2}, U_f = \sqrt{\frac{\tau_{wall}}{\rho}}, \Delta y = \frac{y^+ \mu}{U_f \rho}, \delta = \frac{0.37L}{Re^{1/5}}$$

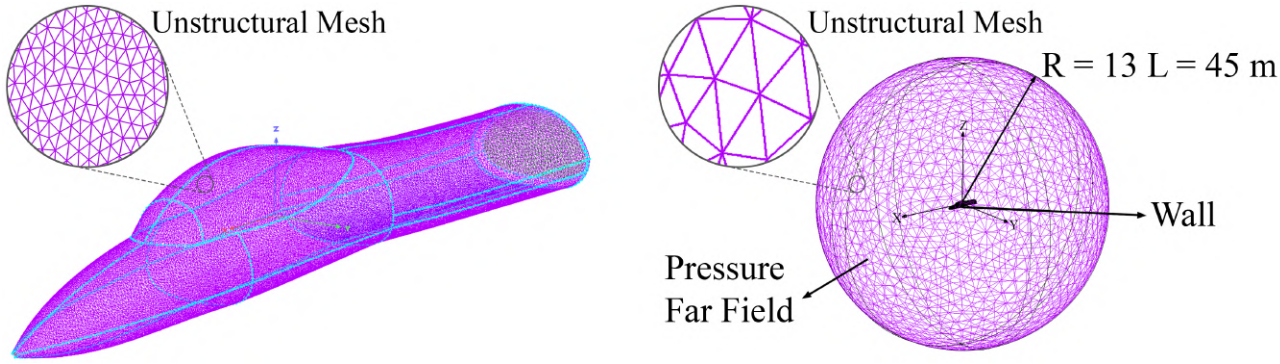

Figure 3: Mesh structure and sphere domian

Following the above formulas, unstructural mesh is applied to all surfaces on the F-16 fighter aircraft. The domain for the geometry is determined and the sphere is chosen as the most suitable domain type. The radius of this sphere is taken as 45 meters. The sphere area is covered with unstructural mesh. This domain and mesh structure are given in Figure 3. Since the boundary layer thickness is different for each

Table 2: Properties of mesh structures

No	Characteristic Length (L) [m]	Mach Number (M)	Reynolds Number (Re)	Velocity (U) [m/s]
1	3.45	0.65	15002584.39	191.82
2		1.05	24245653.01	310
3		1.45	33466822.33	427.9
	y^+	Friction Coefficient (C_f)	Wall Shear Stress (τ_{wall}) [Pa]	Friction Velocity (U_t) [m/s]
1	200	0.00271643	15.60082072	7.069328138
2		0.002467771	37.01600107	10.88928005
3		0.002313709	66.12330702	14.55397755
	Length of First Cell (Δy) [m]	Boundary Layer Thickness (δ) [m]	Time Step Size (Δt) [s]	Courant Number (CFL)
1	0.00125	0.046858416	1×10^{-6}	0.1537
2	0.00081	0.042569058	4×10^{-7}	0.1531
3	0.00061	0.039911488	2.2×10^{-7}	0.1553
	End Time [s]	Maximum Skiwness Angle	Computation Time (CPU × Hour)	Number of Cell
1	0.94	0.795	252×18	2470032
2	0.60	0.808	252×45	2989747
3	0.42	0.813	252×81	3118361

Mach value, computations are made on three different mesh structures. The properties of the created mesh structures are given in Table 2.

3 Computational Methods

The background of the computation methods are the Navier-Stokes equations. The three-dimensional unsteady form of the Navier-Stokes Equations were given below. These equations describe how the velocity, pressure, temperature, and density of a moving fluid are related. These complex equations are extensions of the Euler Equations and include the effects of viscosity on the flow. In theory, the equations are a set of coupled differential equations which could be resolved for a specific flow issue using calculus methods. However, in practice, solving these equations analytically is too difficult.

The Navier-Stokes equations consists of a time-dependent continuity equation for conservation of mass [Eq.(1)], three time-dependent conservation of momentum equations [Eq.(2) for x-momentum, Eq.(3) for y-momentum, Eq.(4) for z-momentum] and a time-dependent conservation of energy equation [Eq.(5)]. In the equations, the x, y, and z are spatial coordinates of some domain, t is the time, P is pressure, and ρ is density. The u is velocity component in the x-direction, the v is velocity component in the y-direction, and the w is velocity component in the z-direction. The q variables are the heat flux components and Pr is the Prandtl Number which is a similarity parameter that is the ratio of the viscous stresses to the thermal stresses. The τ variables are components of the stress tensor.

$$\frac{\partial \rho}{\partial t} + \frac{\partial(\rho u)}{\partial x} + \frac{\partial(\rho v)}{\partial y} + \frac{\partial(\rho w)}{\partial z} = 0 \tag{1}$$

$$\frac{\partial(\rho u)}{\partial t} + \frac{\partial(\rho u^2)}{\partial x} + \frac{\partial(\rho uv)}{\partial y} + \frac{\partial(\rho uw)}{\partial z} = -\frac{\partial P}{\partial x} + \frac{1}{Re}\left[\frac{\partial \tau_{xx}}{\partial x} + \frac{\partial \tau_{xy}}{\partial y} + \frac{\partial \tau_{xz}}{\partial z}\right] \tag{2}$$

$$\frac{\partial(\rho v)}{\partial t} + \frac{\partial(\rho uv)}{\partial x} + \frac{\partial(\rho v^2)}{\partial y} + \frac{\partial(\rho vw)}{\partial z} = -\frac{\partial P}{\partial y} + \frac{1}{Re}\left[\frac{\partial \tau_{xx}}{\partial x} + \frac{\partial \tau_{xy}}{\partial y} + \frac{\partial \tau_{xz}}{\partial z}\right] \tag{3}$$

$$\frac{\partial(\rho w)}{\partial t} + \frac{\partial(\rho uw)}{\partial x} + \frac{\partial(\rho vv)}{\partial y} + \frac{\partial(\rho w^2)}{\partial z} = -\frac{\partial P}{\partial z} + \frac{1}{Re}\left[\frac{\partial \tau_{xx}}{\partial x} + \frac{\partial \tau_{xy}}{\partial y} + \frac{\partial \tau_{xz}}{\partial z}\right] \tag{4}$$

$$\frac{\partial(E_{Total})}{\partial t} + \frac{\partial(uE_{Total})}{\partial x} + \frac{\partial(vE_{Total})}{\partial y} + \frac{\partial(wE_{Total})}{\partial z} = -\frac{\partial uP}{\partial x} - \frac{\partial vP}{\partial y} - \frac{\partial wP}{\partial z} - \frac{1}{RePr}\left[\frac{\partial q_x}{\partial x} + \frac{\partial q_y}{\partial y} + \frac{\partial q_z}{\partial z}\right] + \frac{1}{Re}\left[\frac{\partial}{\partial x}(u\tau_{xx} + v\tau_{xy} + w\tau_{xz}) + \frac{\partial}{\partial y}(u\tau_{xy} + v\tau_{yy} + w\tau_{yz}) + \frac{\partial}{\partial z}(u\tau_{xz} + v\tau_{yz} + w\tau_{zz})\right] \tag{5}$$

The terms found on the left side of the momentum equations are referred to as the convection terms within the equations. Convection is a physical occurrence in a gas flow wherein a certain attribute is conveyed through the organized movement of the flow. The components situated on the right side of the momentum equations, which are multiplied by the inverse Reynolds number, are known as the diffusion terms. Diffusion is a physical occurrence that takes place in a gas flow where a certain attribute is conveyed through the random movement of gas molecules. The process of diffusion is connected to the stress tensor and the viscosity of the gas. Turbulence and the formation of boundary layers are the consequences of diffusion in the flow.

All computations are performed in OpenFOAM, an open source software. OpenFOAM has an extensive range of features to solve anything from complex fluid flows involving chemical reactions, turbulence and heat transfer, to acoustics, solid mechanics and electromagnetics.

The density based implicit transient solver with Wilcox k-ω, SST k-ω RANS turbulence model and SST k-ω DES turbulence model are used for the computations. Implicit, second order, transient, boundedness, and conditionally stable Crank Nicolson numerical computation method is used as time scheme. Limited Gaussian linear method is used as the gradient scheme. In addition, second order, unbounded Gauss linear upwind method by using upwind interpolation weights with an explicit correction based on the local cell gradient is chosen as divergence scheme.

The libAcoustics library is used in the aeroacoustic solutions obtained by the Ffowcs Williams-Hawkings (FW-H) post processing method in OpenFOAM. A commercial software, ANSYS Fluent, is used for aeroacoustic solutions obtained by another post processing method, Fast-Fourier Transfer (FFT). A total of nine computations are performed for this project.

3.1 The k-ω Turbulence Model

There are two-equation in k-ω model and it is y^+ insensitive. These equation are transport equations and they represent the turbulent properties of the flow. The first equation is turbulent kinetic energy, k. The second equations is the specific dissipation, ω. ω determines the scale of the turbulence, whereas equation, k, determines the energy in the turbulence. Eq.(6) and Eq.(7) are the closure equations of the turbulence situation using Reynolds average. They kind of represent the generation and destruction of turbulence. Also, linear models use the Boussinesq assumption for the constitutive relation [25, 27].

$$\rho\frac{\partial k}{\partial t} + \rho\Delta.(\bar{u}k) = \tau\Delta\bar{u} - \beta^*\rho k\omega + \rho\Delta[(\nu + \sigma^*\nu_t)\Delta k] \tag{6}$$

$$\rho\frac{\partial \omega}{\partial t} + \rho\Delta.(\bar{u}\omega) = \gamma\frac{\omega}{k}\tau\Delta\bar{u} - \beta\rho\omega^2 + \rho\Delta[(\nu + \sigma^*\nu_t)\Delta\omega] \tag{7}$$

$$\Delta = \frac{\partial}{\partial x_j}, P = \tau\Delta\bar{u} = \tau_{ij}\frac{\partial u_i}{\partial x_j}$$

Linear models also use the Boussinesq eddy viscosity assumption, Eq.(8) and Eq.(9), for the constitutive relation. Where τ_{ij} is Reynolds stress, μ_t is dynamic eddy viscosity, and δ_{ij} is Kronecker Delta. In addition, if flow is incompressible δ will be $\delta = \frac{\partial u_k}{\partial x_k} = 0$.

$$\tau_{ij} = \mu_t\left(2S_{ij} - \frac{2}{3}\frac{\partial u_k}{\partial x_k}\delta_{ij}\right) - \frac{2}{3}\rho k\delta_{ij} \tag{8}$$

$$S_{ij} = \frac{1}{2}\left(\frac{\partial u_i}{\partial x_j} + \frac{\partial u_j}{\partial x_i}\right) \tag{9}$$

This model uses the Eq.(10) and Eq.(11) relation for the kinematic eddy viscosity and dynamic eddy viscosity, respectively.

$$\nu_t = \frac{k}{\omega} \tag{10}$$

$$\mu_t = \frac{\rho k}{\omega} \tag{11}$$

Clouser coefficients and auxilary relation are as follows.

$$\gamma = \frac{5}{9}, \beta = \frac{3}{40}, \beta^* = \frac{9}{100}, \sigma = \frac{1}{2}, \sigma^* = \frac{1}{2}$$

$$\epsilon = \beta^*\omega k, l = \frac{\sqrt{k}}{\omega}$$

Boundary conditions and initial conditions definition are required each equation. k-ω turbulunce model use wall function and resolve the boundary layer. Moreover, the law-of-the-wall use to specify the boundary condition for the dependent variables. There are different wall function equations for each turbulence model formulation. One can use the following boundary values at the walls for the solution of the boundary layer.

$$\omega_{wall} = 10\frac{6\nu}{\beta y^2}, k_{wall} = 0$$

Where $\beta = 0.075$ and y is the distance of the first cell center normal to the wall. The following equations can be used as boundary values for the far field [26].

$$\omega_{farfield} = \frac{\rho k}{\mu}\left(\frac{\mu_t}{\mu}\right)^{-1}, k_{farfield} = \frac{3}{2}(UI)^2$$

Where $\frac{\mu_t}{\mu}$ is the viscosity ratio, and $I = \frac{u^{'}}{\bar{u}}$ is the turbulence intensity. The values in Table 3 are taken as the reference for the viscosity ratio and the turbulence intensity values for the computations performed in this project.

Table 3: Reference values for the viscosity ratio and turbulence intensity

Coefficient	Low	Medium	High
Turbulence Intensity (I)	0.01	0.05	0.1
Viscoity Ratio (μ_t/μ)	1	10	100
Descriptions	External flow around cars, ships, submarines, and aircrafts.	Flow in not-so-complex devices like large pipes, fans, ventilation flows, wind tunnels, or low speed flows.	High-speed flow inside complex geometries like heat-exchangers and rotating machinery (turbines and compressors).

Finally, k-ω turbulence model is suitable for complex boundary layer flows under adverse pressure gradient (APG) and separation (external aerodynamics and turbo machinery).

3.2 The Shear Stress Transport (SST) k-ω Turbulence Model

Shear Stress Transport (SST) k-ω model is the most successful among Eddy Viscosity Models (EVM). This model consists blending functions, various closure coefficients, and auxiliary relations. A lot of the

coefficients used in this model are computed by a blend function between the respective constants of the k-ϵ and the k-ω turbulence models. The most efficient and commanly used RANS/Unsteady RANS (URANS) turbulence model and it is y^+ insensitive. The SST k-ω turbulence model like k-ω model is a two-equation eddy-viscosity model. This model is almost the same as the k-ω model. Just one constant (σ_{k1}) and the expression for turbulent eddy viscosity are different. The SST formulation combines the two models.

These models are k-ω model and k-ϵ model. The two equations turbulent kinetic energy, k and specific dissipation, ω are given as Eq.(12) and Eq.(13), respectively [14, 15].

$$\rho\frac{\partial k}{\partial t} + \rho\Delta.(\bar{u}k) = \tau\Delta\bar{u} - \beta^*\rho k\omega + \rho\Delta[(\nu + \sigma_k\nu_t)\Delta k] \tag{12}$$

$$\rho\frac{\partial \omega}{\partial t} + \rho\Delta.(\bar{u}\omega) = \frac{\gamma}{\nu_t}\tau\Delta\bar{u} - \beta\rho\omega^2 + \rho\Delta[(\nu + \sigma_w\nu_t)\Delta\omega] + 2(1-F_1)\rho\frac{\sigma_{\omega,2}}{\omega}\Delta k\Delta\omega \tag{13}$$

The use k-ω formulation in the inner region of the boundary layer makes the model can be used all the way down to the wall through the viscous sublayer. In addition, model switches to k-ϵ behaviour in the free stream and thereby avoids the common k-ω problem that the model is too sensitive to the inlet free stream turbulence properties. SST k-ω model show accurate behaviour in APG and separating flow. However, it produces a large turbulence in regions with large normal strain, like stagnation regions and regions with strong acceleration. Moreover, linear models use the Boussinesq eddy viscosity assumption Eq.(14) and Eq.(15), for the constitutive relation, as in k-ω model. Again in this model, where τ_{ij} is Reynolds stress, μ_t is dynamic eddy viscosity, and δ_{ij} is Kronecker Delta [5].

$$\tau_{ij} = \mu_t\left(2S_{ij} - \frac{2}{3}\frac{\partial u_k}{\partial x_k}\delta_{ij}\right) - \frac{2}{3}\rho k\delta_{ij} \tag{14}$$

$$S_{ij} = \frac{1}{2}\left(\frac{\partial u_i}{\partial x_j} + \frac{\partial u_j}{\partial x_i}\right) \tag{15}$$

This model uses the Eq.(16) and Eq.(17) relation for the kinematic eddy viscosity and dynamic eddy viscosity, respectively.

$$\nu_t = \frac{\alpha_1 k}{max(\alpha_1\omega, \Omega F_2)} \tag{16}$$

$$\mu_t = \rho\frac{\alpha_1 k}{max(\alpha_1\omega, \Omega F_2)} \tag{17}$$

Ω in the viscosity equations given below is the magnitude of the vorticity, and W_{ij} is the anti-symmetric part of the velocity gradient. The parameters used in the equations are $\alpha, \sigma_k, \sigma_\omega, \beta, \beta^*$, taken between near wall state (ϕ_1) and far wall state (ϕ_2).

$$\Omega = \sqrt{2W_{ij}W_{ij}}$$

$$W_{ij} = \frac{1}{2}\left(\frac{\partial \bar{u}_i}{\partial x_j} - \frac{\partial \bar{u}_j}{\partial x_i}\right)$$

$$\phi = F_1\phi_1 + (1-F_1)\phi_2$$

$$F_1 = \tanh(arg_1^4), arg_1 = \min\left[\max\left(\frac{\sqrt{k}}{\beta^*\omega d}, \frac{500\nu}{d^2\omega}\right), \frac{4\rho\sigma_{\omega,2}k}{CD_{k\omega}d^2}\right]$$

$$F_2 = \tanh(arg_2^2), arg_2 = \max\left(\frac{2\sqrt{k}}{\beta^*\omega d}\right)$$

$F1$ and F_2 are Blending functions. $F1$ takes a value between 0 and 1: 1 inside the boundary layer and 0 in the free stream. In addition, d is the distance from the wall. If d increases, maximum of arg_1 decreases. Thus, arg_1 diminishes with d, causing F_1 to approach 0 and to approach the far field value. If d decreases, the wall is approached, and in this case the opposite behavior occurs. Also, P_k is the production limiter.

Clouser coefficients and auxilary relations are as follows [16].

$$CD_{k\omega} = \max\left(2\rho\sigma_{\omega,2}\frac{1}{\omega}\Delta k\Delta\omega, 10^{-10}\right)$$

$$P_k = \min\left(\tau\Delta\bar{u}, 10\beta^* k\omega\right)$$

$$\gamma_1 = \frac{5}{9}, \sigma_{k,1} = 0.85, \sigma_{\omega,1} = 0.5, \beta_1 = 0.075$$

$$\gamma_2 = 0.44, \sigma_{k,2} = 1, \sigma_{\omega,2} = 0.856, \beta_2 = 0.0828$$

$$\beta^* = 0.09, \alpha_1 = 0.31$$

Each equation requires the establishment of proper boundary and initial conditions. There are different wall function equations for each turbulence model formulation. One can use the following boundary values at the walls for the solution of the boundary layer.

$$\omega_{wall} = 10\frac{6\nu}{\beta_1 d^2}, k_{wall} = 0$$

The following equations can be used as boundary values for the far field. L is the defining length scale for the particular problem. These terms define the boundary condition values for k and ω.

$$\omega_{farfield} = \frac{5U}{L}, k_{farfield} = 10^{-6}U^2$$

In short, the k-ω SST turbulence model is a variant of k- ω turbulence model that accounts for the transport of the turbulent shear stress and so, offers improved predictions of flow separation under APG. The model differs from k- ω turbulence model in that, a limiter is applied to the eddy and viscosity relationship. In addition, this model was created by combining the k-ω and k-ϵ models. It exhibits k-ω in the inner parts of the boundary layer, whereas k-ϵ behavior in the free stream region. Thus, by taking the good sides of both models, it produces a more accurate results [3].

3.3 Detached Eddy Simulation (DES)

In external flows, different flow behaviors are observed in regions near to the wall (boundary layer) and in other regions. Therefore, different approaches are used for each region to get the optimum results in numerical solutions. Since two different solution methods cannot be used simultaneously in the solution, new methods that combine these two methods have emerged. Detached Eddy Simulation (DES) is one of these methods. This new method performs RANS solutions near the wall and Large Eddy Simulation (LES) solutions in other regions.

The DES approach is derived from the one equation Spart-Allmaras (S-A) model. The distance function, d in the S-A model is obtained by substituting a redefined distance function, $\tilde{d}$ [12, 21]. Where C_{DES} is a constant and Δ is the largest dimension of the mesh cell.

$$\tilde{d} = \min[d, C_{DES}\Delta] = \min\left(\frac{\sqrt{k}}{\beta^*\omega}, C_{DES}\Delta\right)$$

Redefined distance function supply the model to behave as a RANS model in regions near the wall. The DES may be used with any turbulence model that has an suitable defined turbulence length scale model. In this project, the DES approach is applied to the SST k - ω turbulence model. SST k - ω turbulence model uses a turbulence length scale and compares it with the mesh length scale to switch between LES and RANS [22]. Many DES approaches allow regions to be specified as RANS or LES regions explicitly, bypassing the distance function calculation.

3.4 Ffowcs Williams-Hawkings (FW-H) Method

There are two fields for sound, these are the source field and propagation field. However, source field is separated from the propagation field . Source fields are calculated by using Direct Numerical Simulation (DNS), LES, DES, or RANS. There are two main approaches to receive the sound of the far field. Ffowcs Williams-Hawkings (FW-H) is a direct approach that calculates the waves propagating to the far field and uses an integration surface that serves as the source of the wave equation to be solved analytically [11]. Direct approaches include the solution of modified wave equations or linearized Euler equations. The acoustic similarity propagates the sound field analytically by solving the wave equation using the associated Green's function. FW-H method was used in this project [17, 20].

The FW-H equations are the rearranged variant of the governing equations. All flow variables depend on time, but no spatial derivative is required. The solution of the FW-H equation requires surface integrals and volume integrals, but in many cases the surface integrals alone are sufficient for approximation. The FW-H equation can be written as Eq.(18) [8,10]. Where T_{ij} is Lighthill stress tensor, F_i is unsteady force, and Q is unsteady mass. These terms can be written as below.

$$\left(\frac{\partial^2}{\partial t^2} - c^2\frac{\partial^2}{\partial x_i \partial x_i}\right)\left(H(f)\rho^{'}\right) = \frac{\partial^2}{\partial x_i \partial x_i}\left(T_{ij}H(f)\right) - \frac{\partial}{\partial x_i}\left(F_i\delta(f)\right) + \frac{\partial}{\partial t}\left(Q\delta(f)\right) \tag{18}$$

$$T_{ij} = \rho u_i u_j + P_{ij} - c^2\rho^{'}\delta_{ij}$$
$$F_i = \left(P_{ij} + \rho u_i(u_j - v_j)\right)\frac{\partial f}{\partial x_j}$$
$$Q = \left(\rho_0 v_i + \rho(u_i - v_i)\right)\frac{\partial f}{\partial x_i}$$
$$P^{'} = P - P_0$$
$$\rho^{'} = \rho - \rho_0$$
$$P^{'} = c^2(\rho - \rho_0)$$

In these terms, u_i is fluid velocity component in the x_i direction, u_j is velocity component perpendicular to the surface, v_i is surface velocity component in the x_i direction, v_j is surface velocity component perpendicular to the surface, ρ is total density, ρ_0 is free stream density, and c is speed of sound. In addition to these, $P^{'}$ is the sound pressure at the far field, P is total pressure, and P_0 is free stream pressure.

The function $f = 0$ is a surface used for the exterior region ($f > 0$) problem. The Kronecker Delta, δ_{ij} is equal to 1 for $i = j$; otherwise, it is equal to 0. Another term to be defined is the Heaviside function. It is a step function and is denoted by $H(f)$. Heaviside function is equal to 1 when $f > 0$, and it is equal to 0 if $f < 0$. The derivative of the Heaviside function is defined as Dirac Delta and denoted as $\delta(f)$. Dirac Delta is equal to 0 for $f \neq 0$, and it takes a finite value if $f = 0$. Also, compressive stress tensor, P_{ij} is used in this project.

$$H^{'}(f) = \delta(f)$$
$$P_{ij} = P\delta_{ij} - \mu\left[\frac{\partial u_i}{\partial x_j} + \frac{\partial u_j}{\partial x_i} - \frac{2}{3}\frac{\partial u_k}{\partial x_k}\delta_{ij}\right]$$

The FW-H equation given in Eq.(18) is solved using Green's function method. Also, the Green function gives the solution $\rho^{'}$ which is the density at the far field.

$$c^2 = \frac{\partial p^{'}}{\partial \rho^{'}}, G = \frac{\delta(g)}{4\pi r}$$

Surface and volume integrals are used for the complete solution. Surface integrals represent data from monopole, dipole, and quadrupole sources, while volume integrals represent quadrupole data outside the sources.

Assuming that the surface f is placed on the body and the body itself cannot penetrate, the classical FW-H equation is obtained and the nonlinear propagation effect is explained by the quadrupole volume term. Moving the surface f away from the body yields a kind of mixed formulation. Part of the nonlinearity is explained by the quadrupole volume term and part by the surface integral. If the surface is far enough from the body, the Lighthill stress tensor outside f is negligible. The intregral solution can be written as Eq.(19) and Eq.(20) [2, 9, 11].

$$P^{'}(x_i,t) = P^{'}_T(x_i,t) + P^{'}_L(x_i,t)$$

$P^{'}_T(x_i,t)$ and $P^{'}_L(x_i,t)$ are thickness term and loading term, respectively.

$$4\pi P^{'}_T(x_i,t) = \int_{f=0}\left[\frac{\rho_0(\dot{U}_n + U_{\dot{n}})}{r(1-M_r)^2}\right]_{ret} dS + \int_{f=0}\left[\frac{\rho_0 U_n\left(r\dot{M}_r + c(M_r - M^2)\right)}{r^2(1-M_r)^2}\right]_{ret} \tag{19}$$

$$4\pi P^{'}_T(x_i,t) = \frac{1}{c}\int_{f=0}\left[\frac{\dot{L}_r}{r(1-M_r^2)}\right]_{ret} dS + \int_{f=0}\left[\frac{L_r - L_M}{r^2(1-M_r)^2}\right]_{ret} dS + \frac{1}{c}\int_{f=0}\left[\frac{L_r\left(r\dot{M}_r + c(M_r - M^2)\right)}{r^2(1-M_r)^3}\right]_{ret} dS \tag{20}$$

The dot means source-time differentiation. The subscripted quantities found in the equations are given below.

$$U_i = u_i + \left[\left(\frac{\rho}{\rho_0}\right) - 1\right](u_i - v_i)$$
$$L_i = P_{ij}\hat{n} + \rho u_i(u_j - v_j)$$
$$L_r = \vec{L}.\vec{r} = L_i r_i, U_n = \vec{U}.\vec{n} = U_i n_i, L_M = \vec{L}.\vec{M} = L_i M_i$$
$$M_i = \frac{v_i}{c} M_r = \frac{v_i r_i}{c}$$
$$\tau = t - \frac{r}{c}$$
$$SPL = 20\log(\frac{P}{P_{ref}})dB$$

The ret, τ under the square brackets in the equations means that the integrals are calculated in retarded time. τ relates to r, t and c, where t is observer time, r is distance to the observer. The sound pressure P, either the Sound Pressure Level (SPL), measured in decibels (dB). Where P_{ref} is reference sound pressure, and it is usually 2×10^{-5} for air.

3.5 Fast-Fourier Transfer (FFT) Method

This method has an important place in acoustic calculations. It basically converts a signal string into components and gives information about the frequency of the signal. It can convert signals from time domain to frequency domain or from frequency domain to time domain. In this project, commercial software ANSYS Fluent is used for this transformation. The time-pressure values obtained from the computation results are uploaded to ANSYS Fluent and the conversion is made by enabling the "Acoustics Analysis" box in the Fast-Fourier Transfer (FFT) section.

As a result of the transformation, SPL-frequency values are obtained. Twelve microphones and twelve probes are placed at the same points on the canopy. The locations of the placement points are given in Figure 5. SPL-frequency data are obtained from the microphones, and time-pressure data are obtained from the probes. Microphones and probes are grouped among themselves in order to better interpret the computation outputs. P1-P4 are grouped as the front probes/microphones, P5-P8 as middle probes/microphones, and P9-P12 as back probes/microphones.

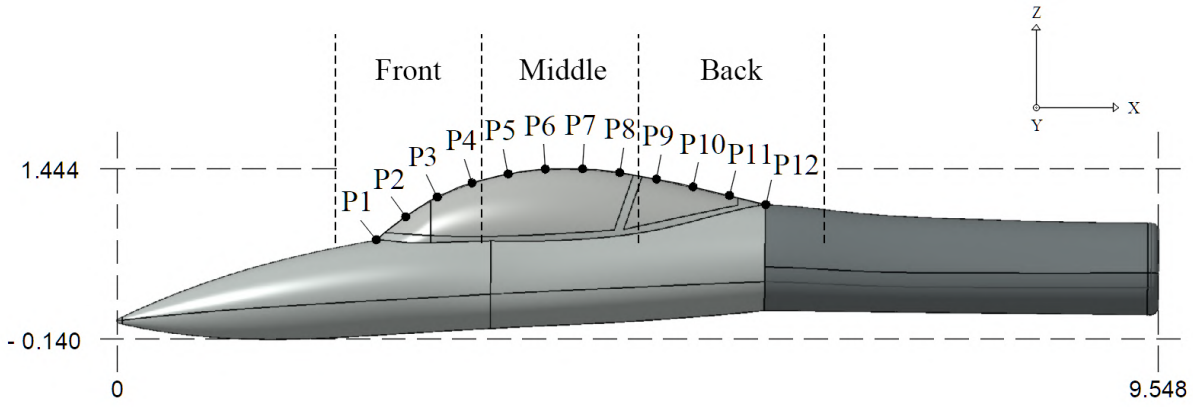

Figure 4: Location of probes and microphones

As mentioned above, there are two areas for noise, the source field and the propagation field. For source field computitons, probes are placed on the noise source and the pressure values measured by the probes are found using DNS, LES, DES, or RANS computiton methods. Afterwards, these values are processed to reach the desired noise values. For propagation field computitons, microphones are placed at points far from the noise source and noise values are directly obtained using the FW-H computiton method. In this study, the results that would be obtained by placing both a probe and a microphone in the source field were wondered, and the results of these two different solution methods in the source area were evaluated.

4 Numerical Results

Since the solution schemes used in the computations are tested in our previous studies and gave realistic results, they are also used in this project, relying on their accuracy. The output of the study used as the schemes validation case are given in the Table 4. Experimental data is taken from Sarlak study [19].

Table 4: Output of the schemes validation case

Airfoil	NREL S826	**Divergence Scheme**	Gauss linearUpwind limited
Chord Length [m]	0.1	**Time Scheme**	CrankNicolson 0
Re	100000	**C_d (Calculated)**	0.045053
Velocity [m/s]	15	**C_d Error Rate [%]**	4.1727
Angle of Attack [°]	10	**C_l (Calculated)**	1.27873
Boundary Conditions	Free Stream	**C_l Error Rate [%]**	0.4501

Similarly, aeroacoustics computations were tested in our previous studies and gave realistic results, they are also used in this project, relying on their accuracy. Details of the study used as the aeroacoustics validation case are given in Table 5a and Table 5b.

Table 5: Details of the aeroacoustics validation case

(a)

Airfoil	NACA 0012
Chord Length [m]	0.3048
Span Length [m]	0.03048
Re	1500000
Velocity	71.3
Angle of Attack [°]	0°, 14.4°
Microphone Location (Above) [m]	1.219

(b)

Boundary Conditions	**U**	**p**	**T**	**nut**
Farfield	Free Stream Velocity	Free Stream Pressure	fixedValue	Calculated
Airfoil	noSlip	zeroGradient	zeroGradient	nutkWallFunction / nutkRoughWallFunction
Sym	symmetry	symmetry	symmetry	symmetry

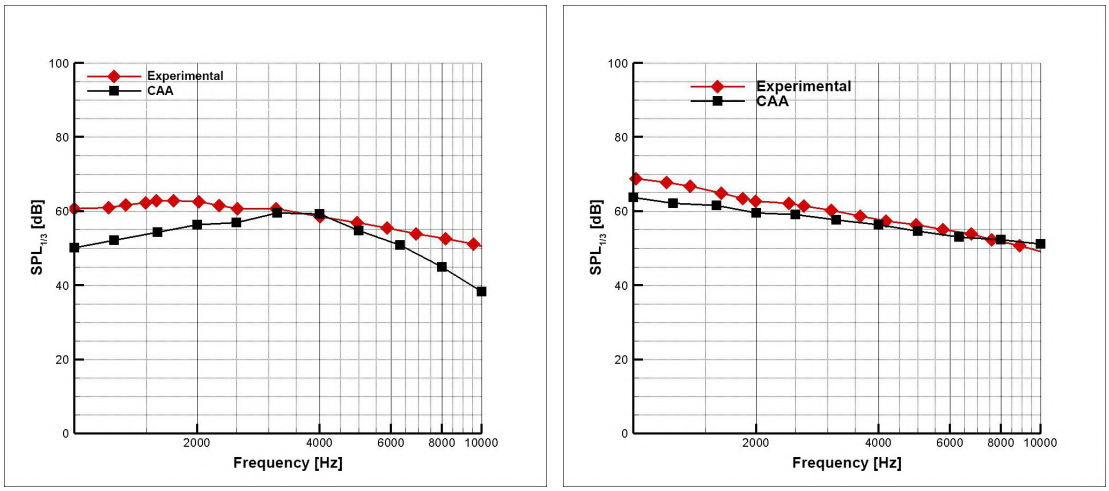

(a) (b)

Figure 5: (a) Output of the 0° angle of attack aeroacoustics validation case (b) Output of the 14.4° angle of attack aeroacoustics validation case

In addition, the outputs of the study used as the aeroacoustics validation case are also given in Figure 5a and Figure 5b. Experimental data are taken from the Brooks study [1].

4.1 Probe Results

One representative was selected for each region (front, middle and back) from the probes placed on the canopy. In this way, it was intended to simplify the noise data obtained and facilitate interpretation. These representatives are the probes where the slope on the canopy is the highest ($P2 - P11$) and zero ($P6$).

4.1.1 Different Probe Places

There are total of nine graphs and each graph contains the results obtained from representative probes of the computations and allows these results to be compared. Thus, the results of noise levels in different places on the canopy were examined. The results of the k-ω turbulence model are given in Figure 6, the results of the SST k-ω turbulence model are given in Figure 7, and the results of the DES SST k-ω turbulence model are given in Figure 8.

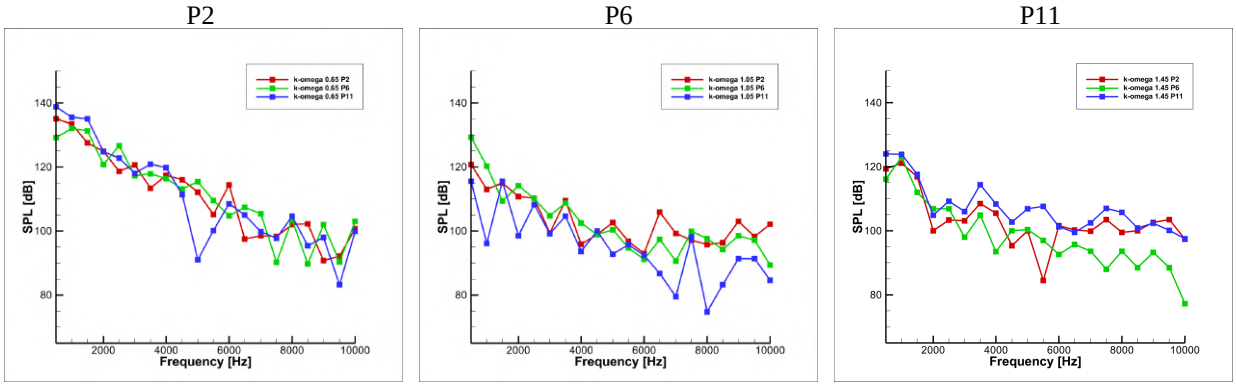

(a) (b) (c)

Figure 6: Different probe place results for k-ω turbulence model

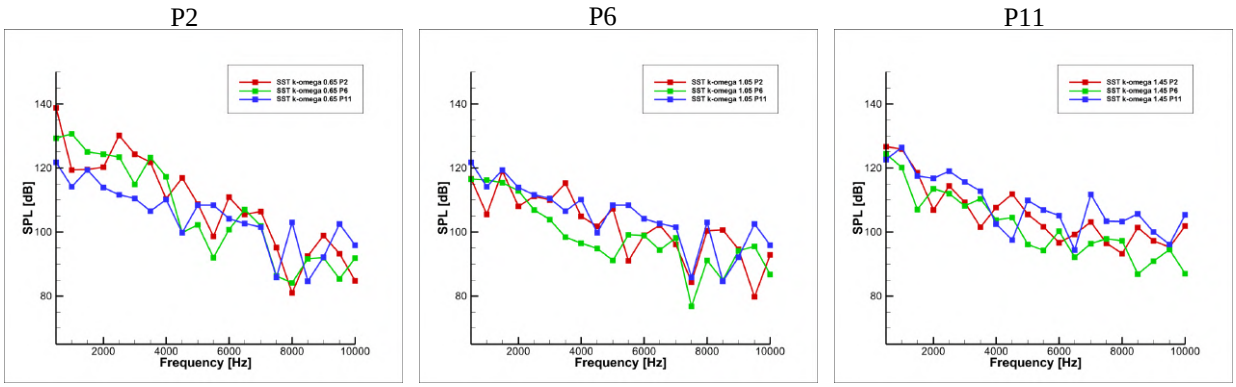

(a) (b) (c)

Figure 7: Different probe place results for SST k-ω turbulence model

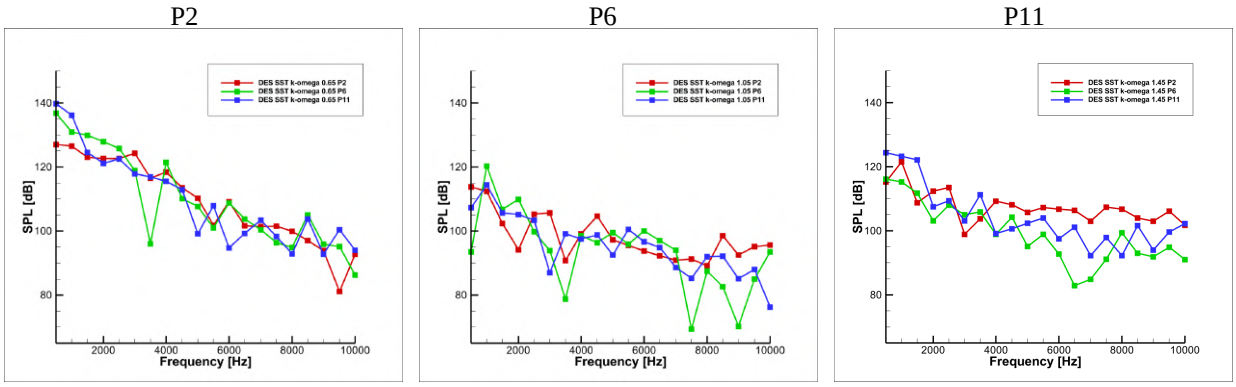

(a) (b) (c)

Figure 8: Different probe place results for DES SST k-ω turbulence model

4.1.2 Same Turbulence Model Different Mach Values

There are total of nine graphs in which turbulence models remain constant and Mach values change. Each graph contains only one of the representative probes. Therefore, remain the turbulence model constant and changing the Mach value enabled the examination of the effect of the Mach value on noise in the same place. Graphs for the k-ω turbulence model, where the probes are $P2$, $P6$ and $P11$ respectively, are given in Figure 9. Likewise, the graphs are given in Figure 10 for the SST k-ω turbulence model and in Figure 11 for the DES SST k-ω turbulence model.

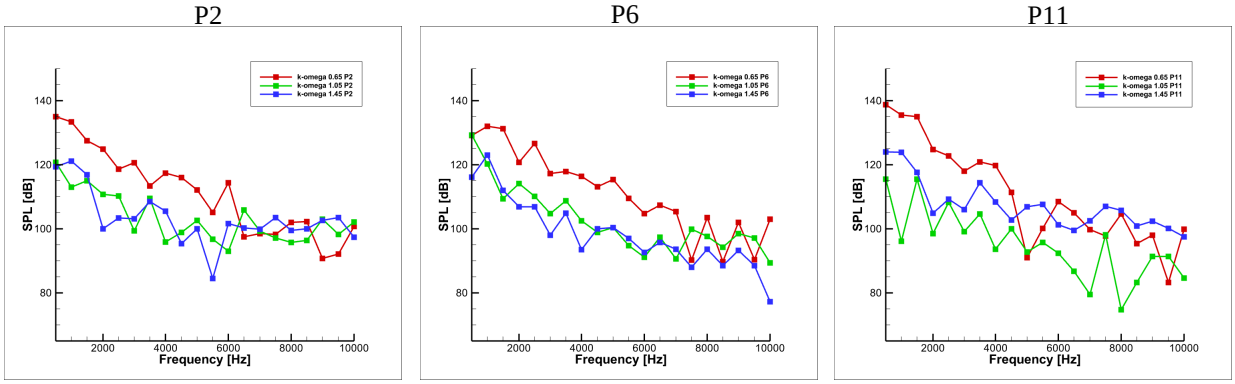

(a) (b) (c)

Figure 9: Same turbulence model different Mach values results for k-ω turbulence model

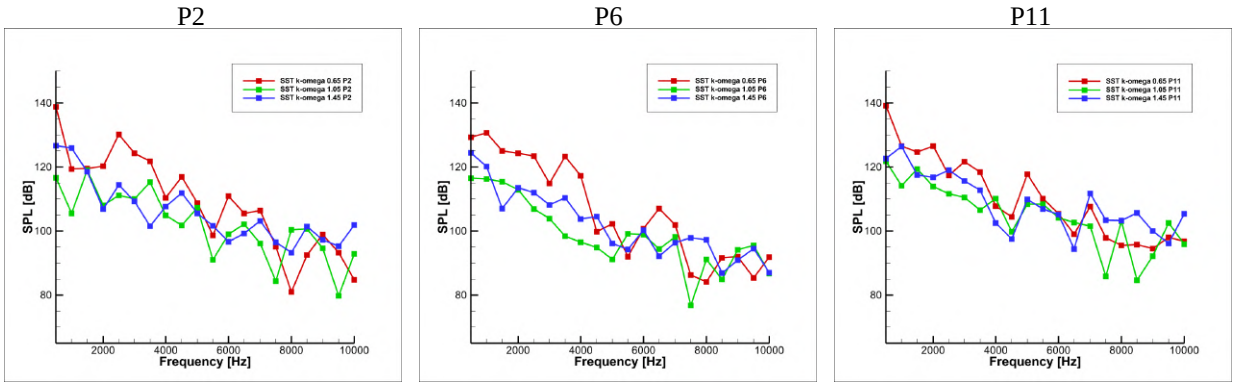

(a) (b) (c)

Figure 10: Same turbulence model different Mach values results for SST k-ω turbulence model

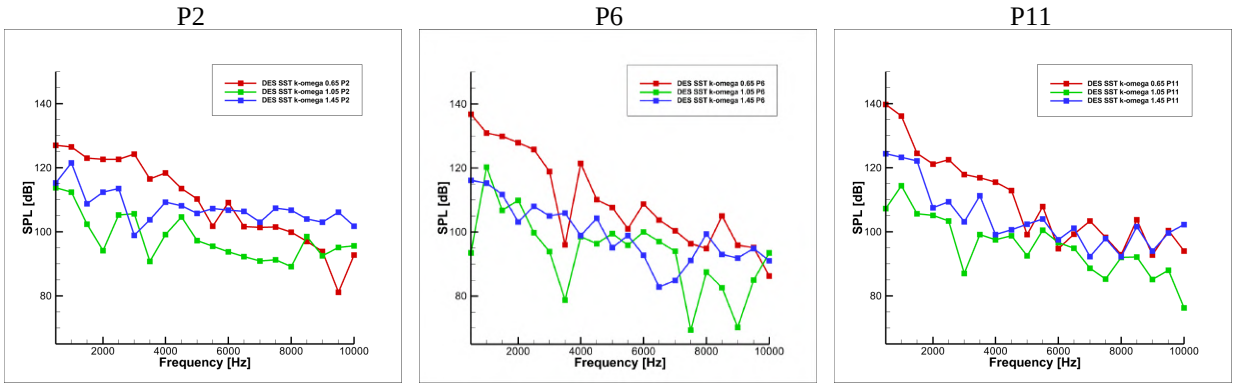

(a) (b) (c)

Figure 11: Same turbulence model different Mach values results for DES SST k-ω turbulence model

4.1.3 Same Mach Value Different Turbulence Models

There are total of nine graphs in which Mach values remain constant and turbulence models change. Each graph contains only one of the representative probes. Therefore, remain the Mach value constant and changing the turbulence model enabled the examination of the effect of the turbulence model on noise in the same place. Graphs for the Mach 0.65, where the probes are $P2$, $P6$ and $P11$ respectively, are given in Figure 12. Likewise, the graphs are given in Figure 13 for the Mach 1.05 and in Figure 14 for the Mach 1.45.

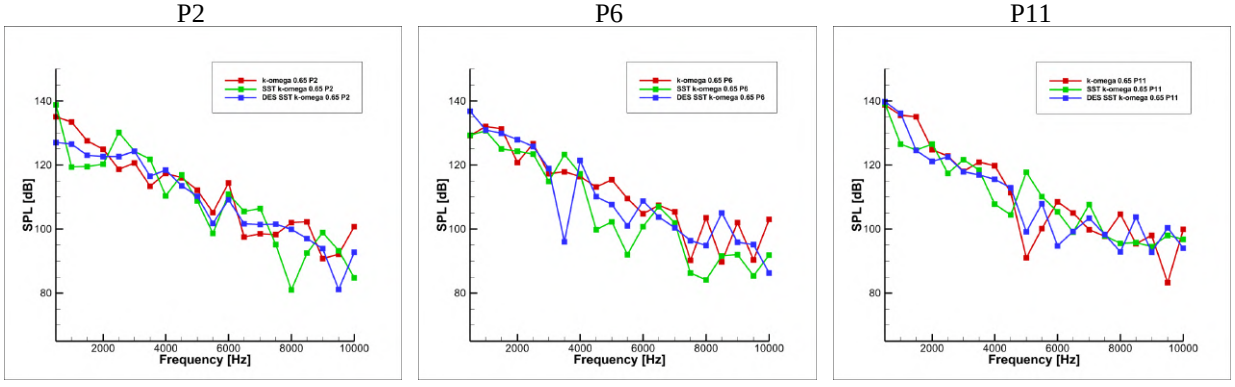

(a) (b) (c)

Figure 12: Same Mach value different turbulence models results for Mach 0.65

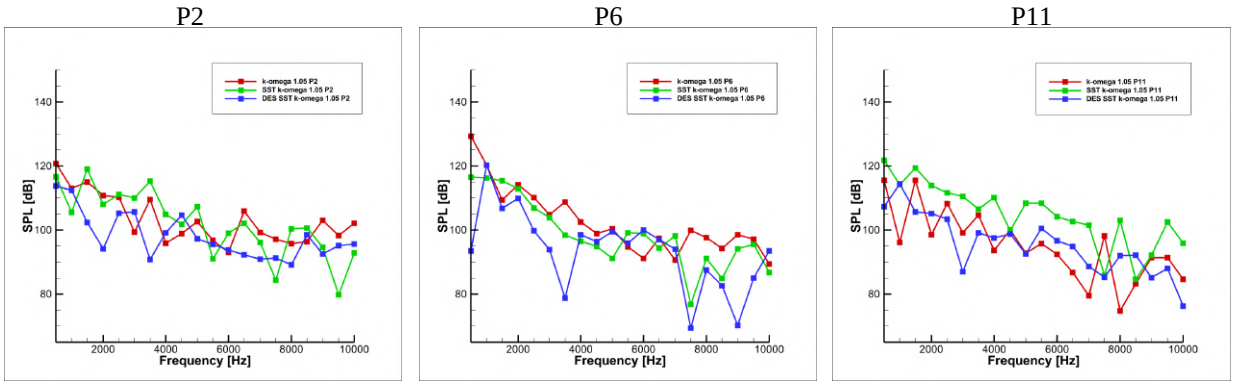

(a) (b) (c)

Figure 13: Same Mach value different turbulence models results for Mach 1.05

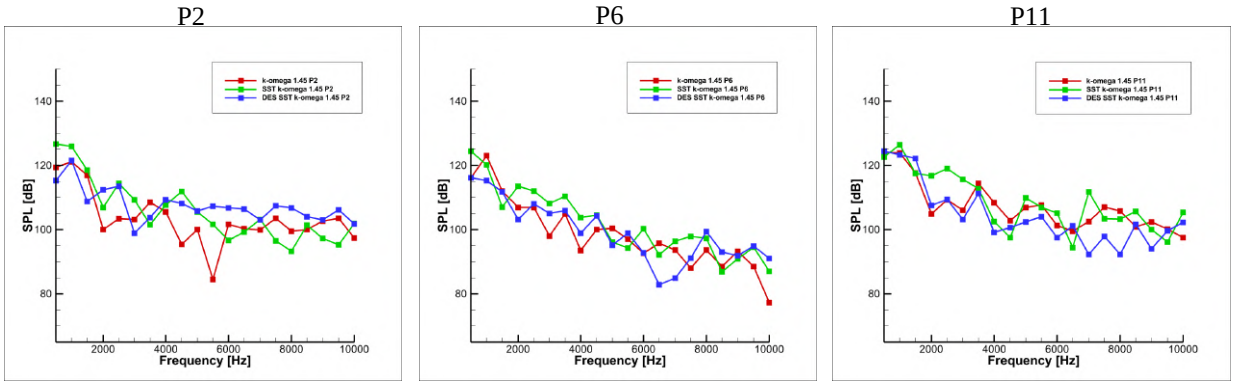

(a) (b) (c)

Figure 14: Same Mach value different turbulence models results for Mach 1.45

4.2 Probe And Microphone Comparison Results

All probe and microphone comparison results are given for Mach 0.65, Mach 1.05, Mach 1.45 and each turbulence model. Data obtained using the FW-H method is indicated by the letter M, and the data obtained using the FFT method is indicated by the letter P. Since any data cannot be obtained from $P3$ and $P12$ probes, data from ten probes is available for each computation made with FFT. There are twenty seven comparison graphs (Figure 15, 16, 17 for Mach 0.65, Figure 20, 21, 22 for Mach 1.05, and Figure 25, 26, 27 for Mach 1.45) and eighteen contours (Figure 15, 16 for Mach 0.65, Figure 20, 21 for Mach 1.05, and Figure 25, 26 for Mach 1.45), including velocity contours and pressure contours.

4.2.1 Mach 0.65 (Subsonic)

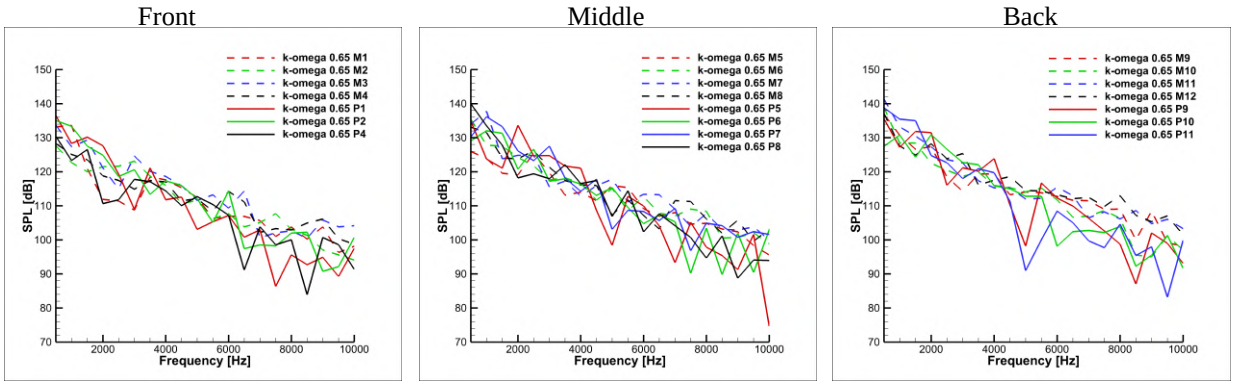

(a) (b) (c)

Figure 15: Plots of all k-ω turbulence model data

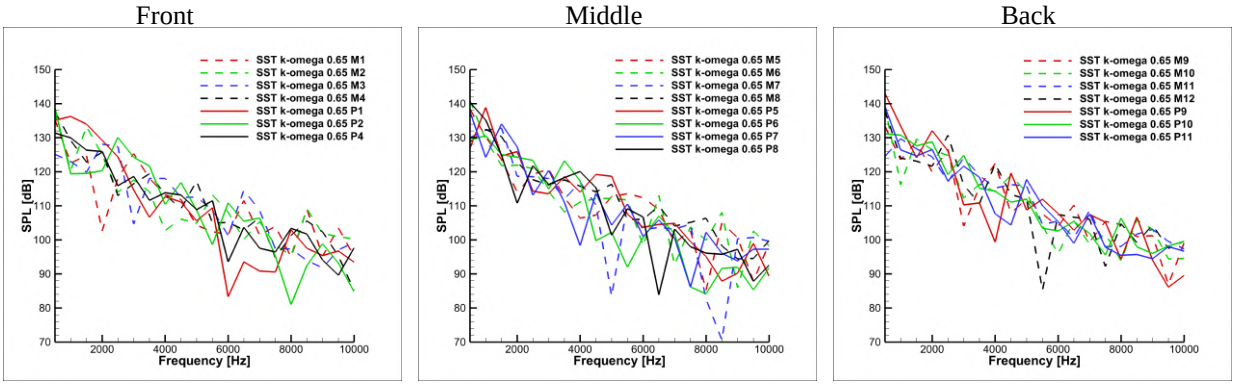

(a) (b) (c)

Figure 16: Plots of all SST k-ω turbulence model data

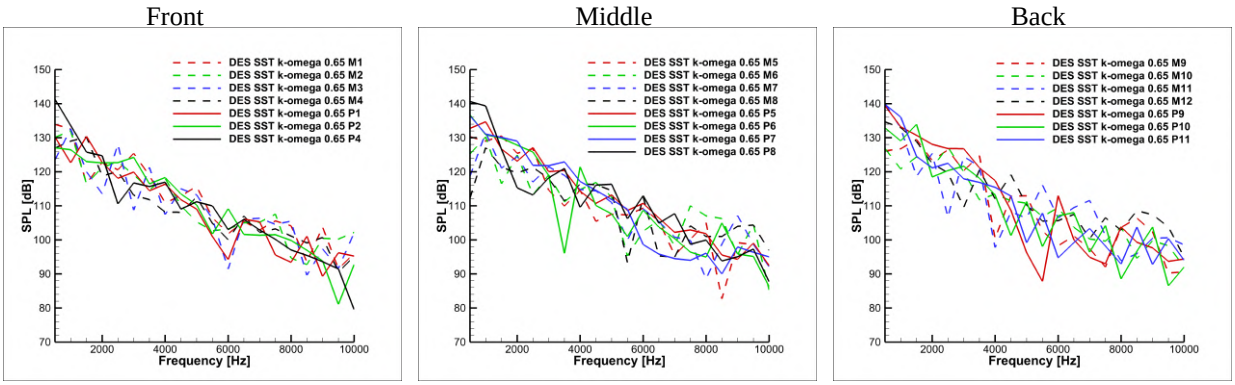

(a) (b) (c)

Figure 17: Plots of all DES SST k-ω turbulence model data

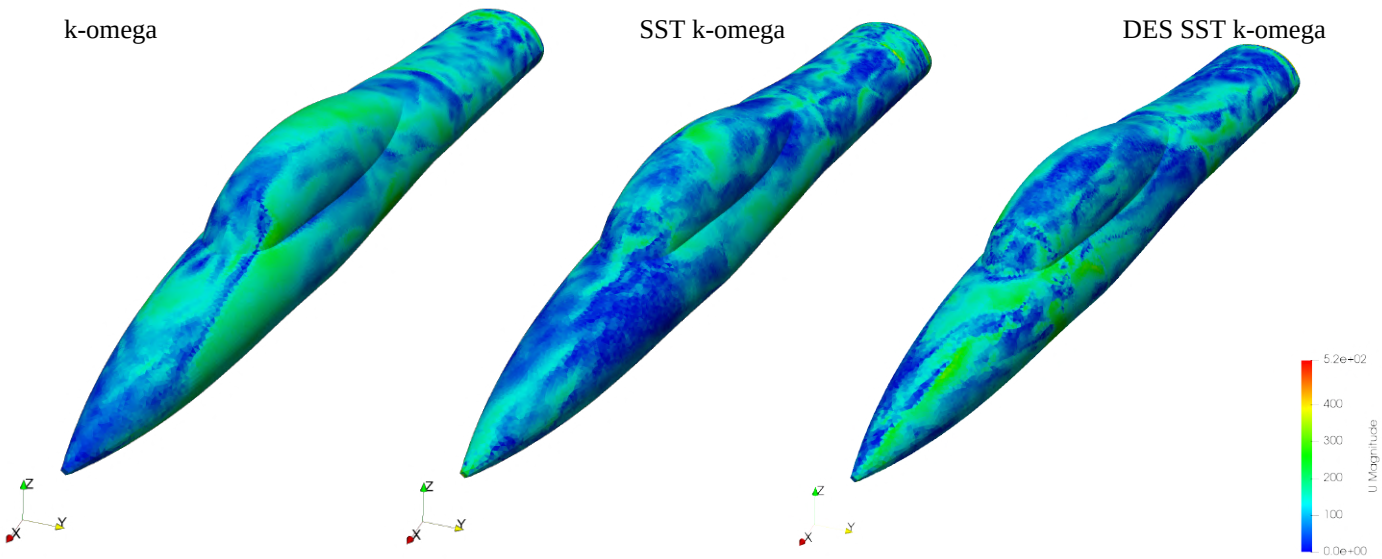

(a) (b) (c)

Figure 18: Velocity distribution of all Mach 0.65 data

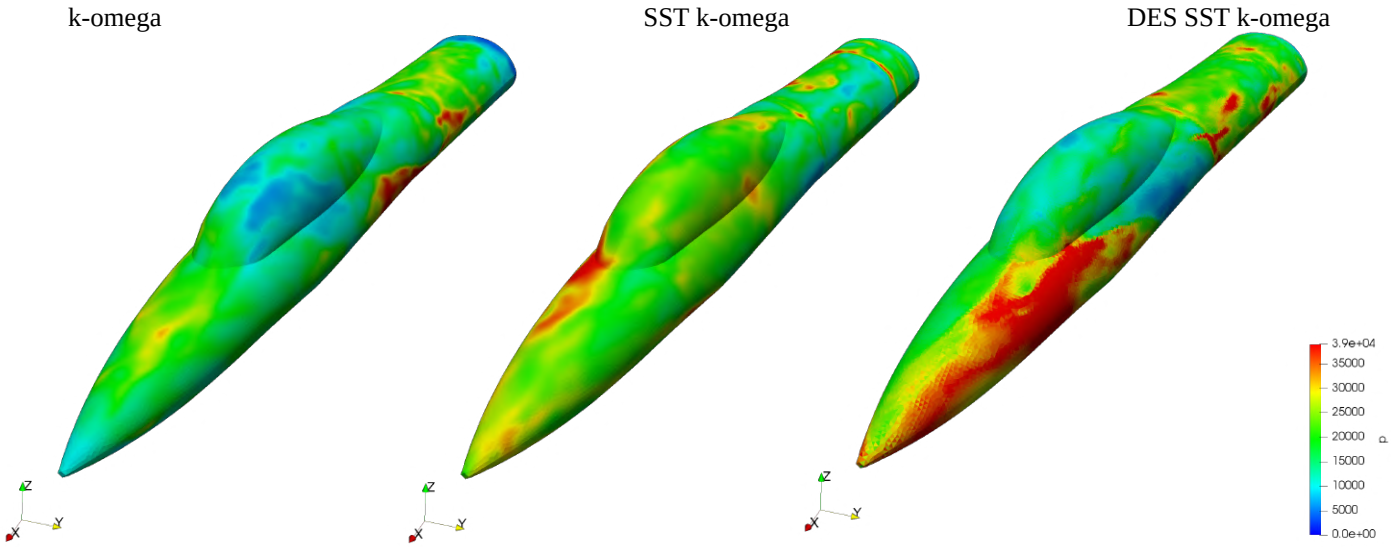

(a) (b) (c)

Figure 19: Pressure distribution of all Mach 0.65 data

4.2.2 Mach 1.05 (Transonic)

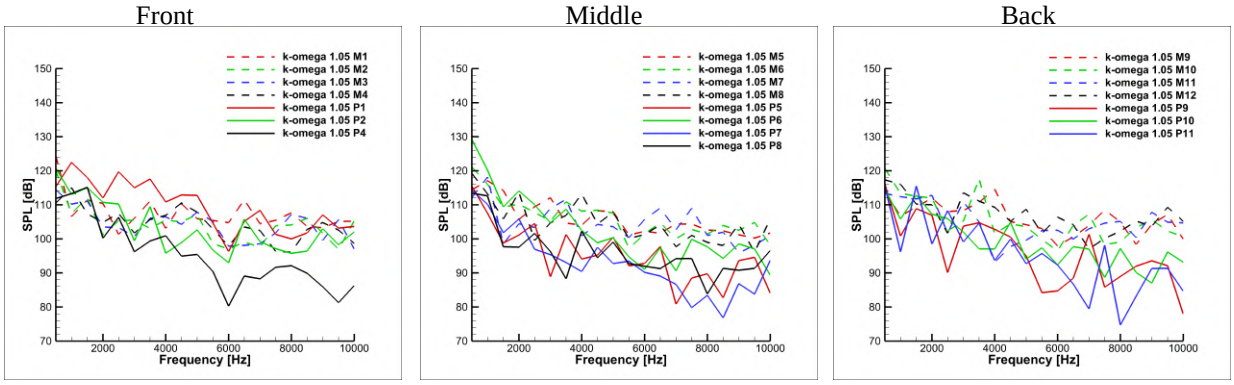

(a) (b) (c)

Figure 20: Plots of all k-ω model data

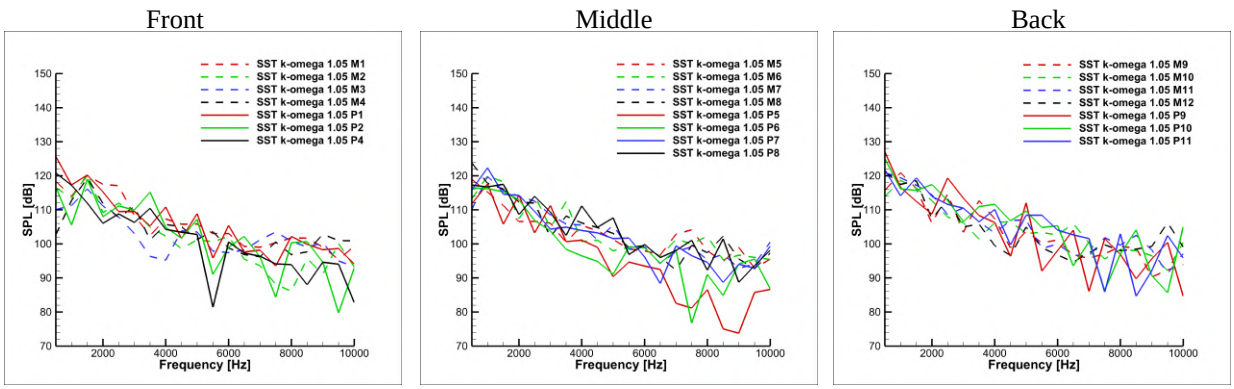

(a) (b) (c)

Figure 21: Plots of all SST k-ω model data

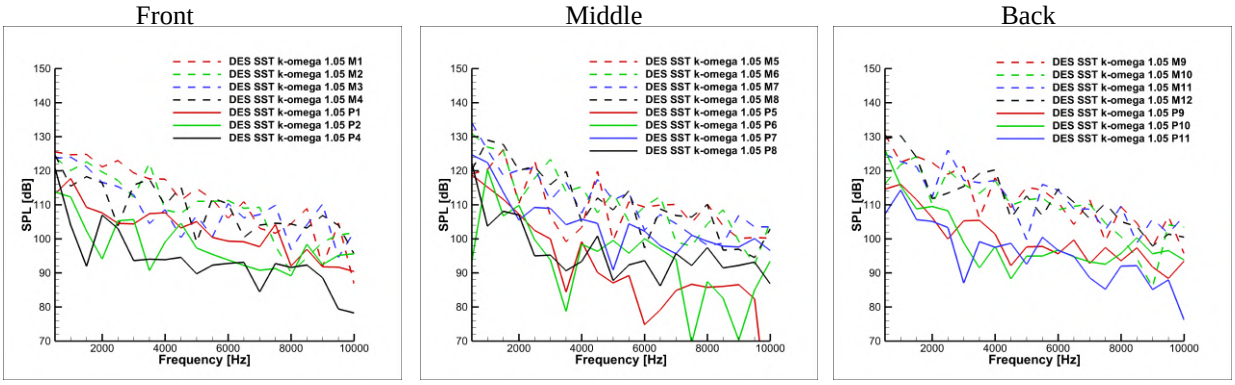

(a) (b) (c)

Figure 22: Plots of all DES SST k-ω model data

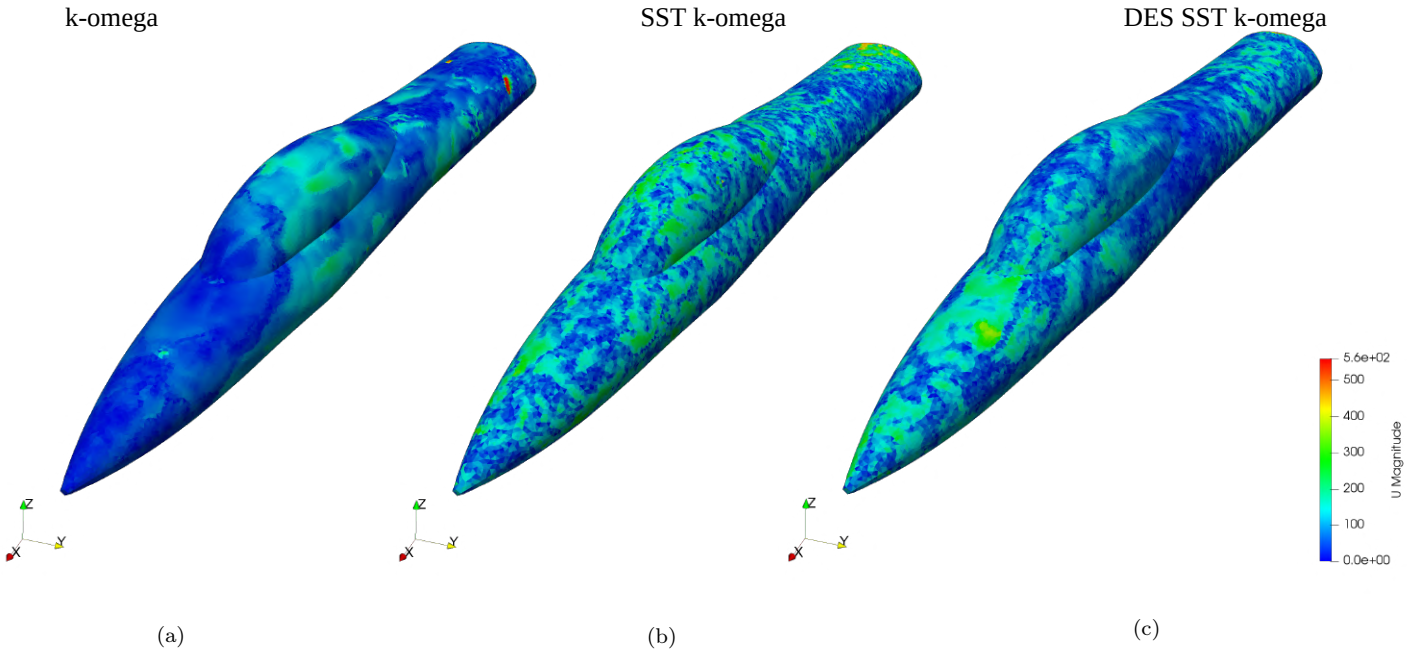

(a) (b) (c)

Figure 23: Velocity distribution of all Mach 1.05 data

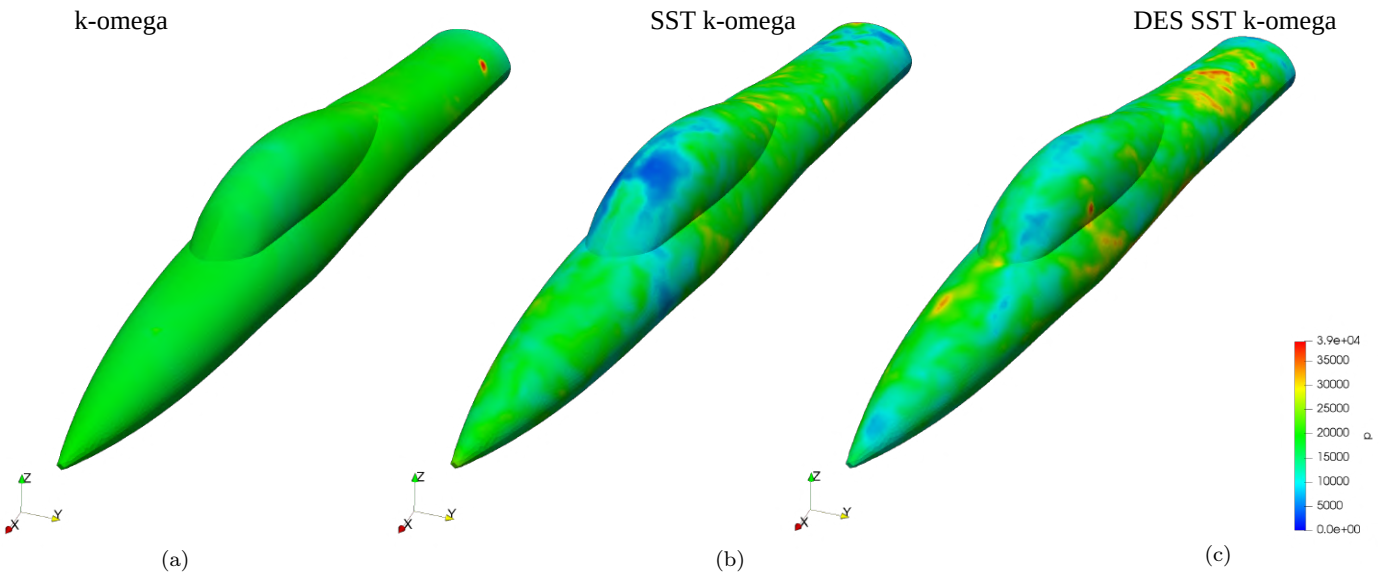

(a) (b) (c)

Figure 24: Pressure distribution of all Mach 1.05 data

4.2.3 Mach 1.45 (Supersonic)

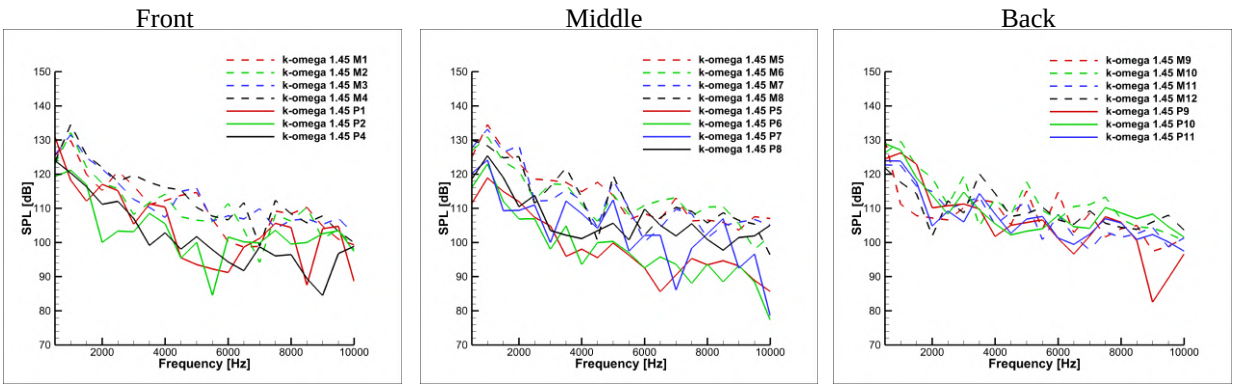

(a) (b) (c)

Figure 25: Plots of all k-ω model data

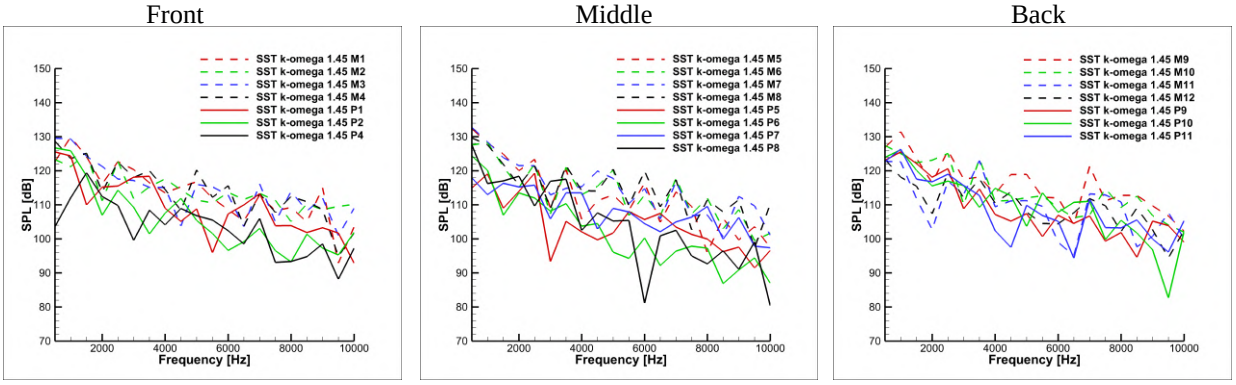

(a) (b) (c)

Figure 26: Plots of all SST k-ω model data

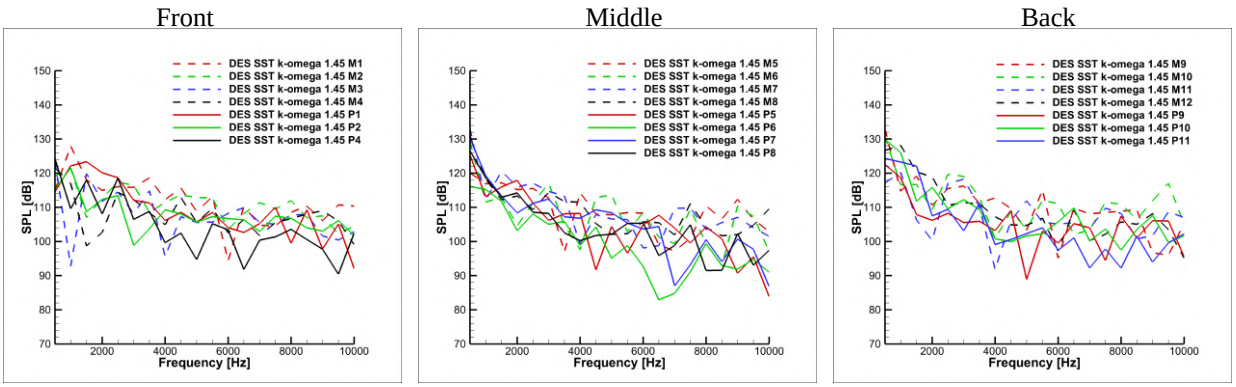

(a) (b) (c)

Figure 27: Plots of all DES SST k-ω model data

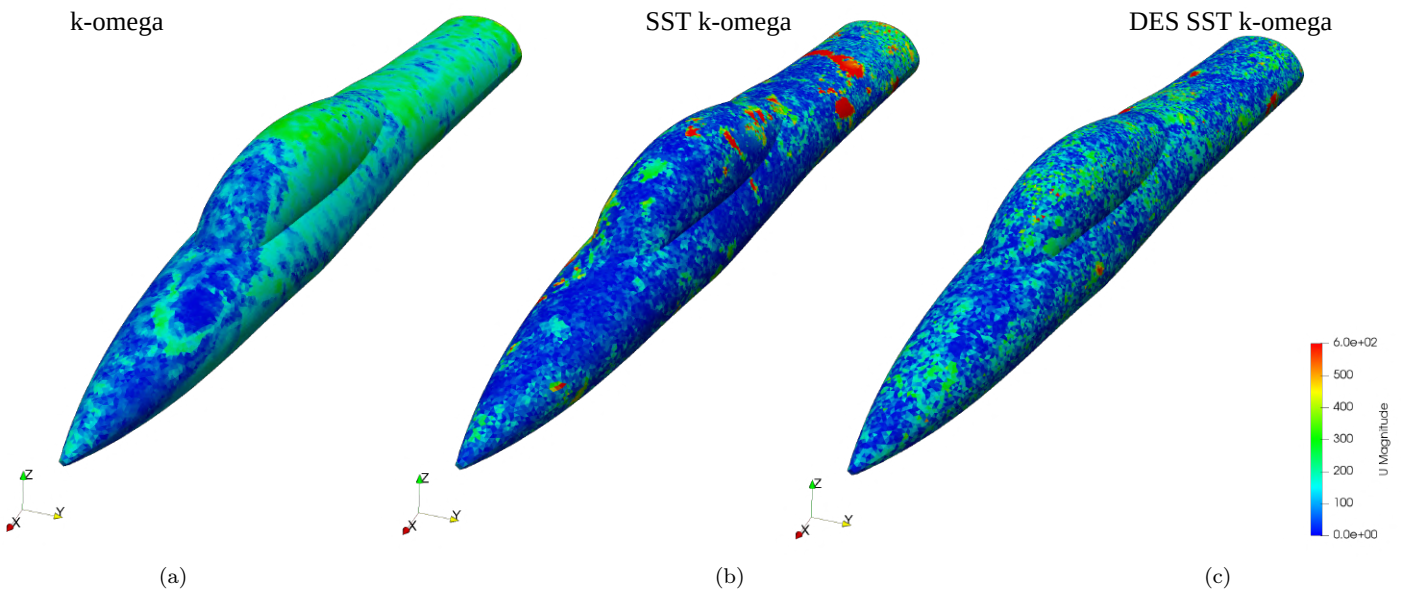

Figure 28: Velocity distribution of all Mach 1.45 data

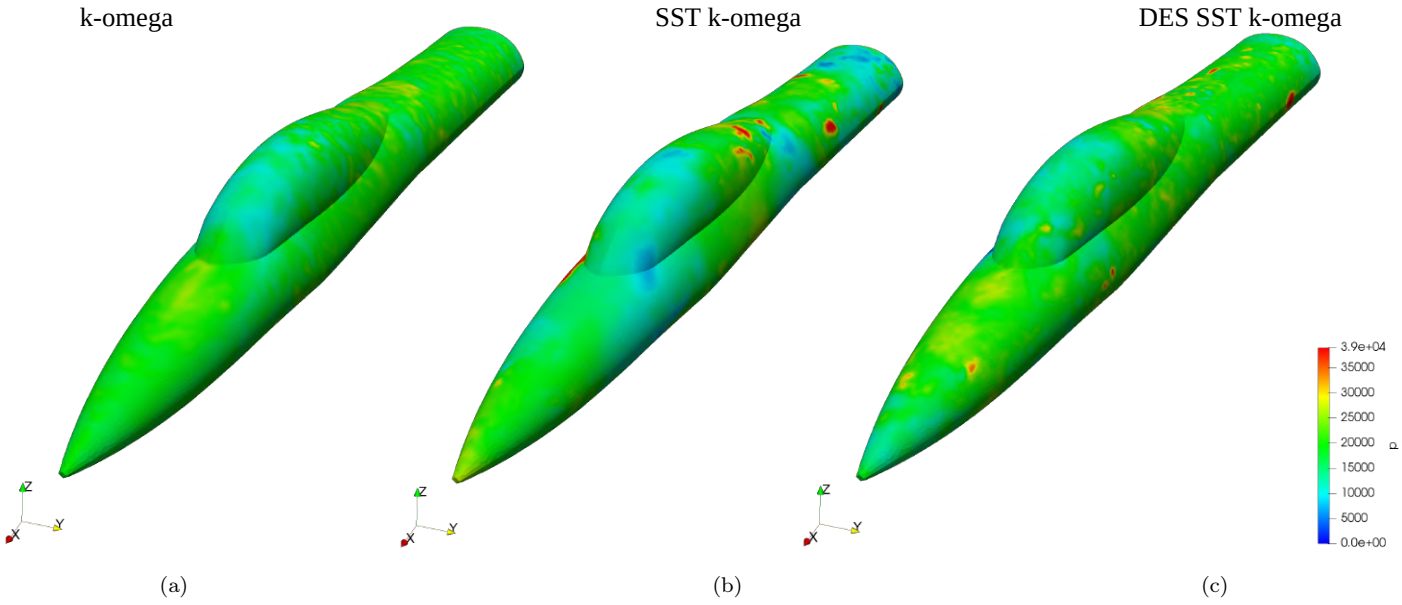

Figure 29: Pressure distribution of all Mach 1.45 data

5 Conclusion and Future Work

In conclusion, it is observed that SPL values between 500 1500 Hz in the computations performed at the Mach 0.65 value mostly vary between 120 140 dB. However, when the computations at Mach 1 05 and Mach 1.45 values are examined, the results are observed that the values obtained in the same frequency range mostly vary between 110 130 dB. As a results, velocity increases, the pressure on the canopy decreases, so the SPL values obtained decrease and a quieter area is formed on the canopy. At the same time, it is observed that SPL values decrease as the frequency values increase. It is thought that the reason for this is the increment in the margin of error in the computations at high frequency values.

In addition, sharper decreases are observed as the frequency values increase in the graphs of Mach 0.65 value computation, while more horizontal transitions are observed in the Mach 1.05 value and Mach 1 45 value computation graphs. Moreover, differences between FW-H and FFT post processing methods are observed in all computations with the largest gap in the DES SST k-ω turbulent model computation at Mach 1.05.

The results obtained are close to the values mentioned in the Introduction section. In addition to this, our industry advisor interpreted that the SPL values at low frequencies in the reflect the real world data. However, since there is no experimental data to compare the obtained computations, it is not possible to tell the best computation method for any Mach value. Based on this interpretations, different studies can be carried out to reduce the noise levels, or the results of this project can be used as a numerical computation data pool to compare with further experimental studies to reach more reliable results.

6 Acknowledgments

For providing the required additional resources and support, I would like to present my deepest thanks to our university rector Prof. Dr. İsmail Koyuncu. I am also immensely thankful to my academic advisor Assoc. Prof. Baha Zafer and industrial advisor Cihad Dikici, with whom we carried out the work within the scope of TUSAŞ Lift Up Graduation Project. Last but not least, I want to thank my friends Mehmet Alim and Selman Kaplan for their support throughout the study, and Serkan Ulugönül for helping prepare the figures used in the study. Moreover, the computing resources used in this study were provided by the Turkish National High Performance Computing Center (UHeM) within the scope of grant number 1012362022.

7 References

[1]Brooks, T.F., Pope, D.S. and Marcolini, M.A. (1989) Airfoil Self-Noise and Prediction. NASA Reference Publication 1218, National Aeronautics and Space Administration, USA.

[2]Di Francescantonio, P. (1997). A NEW BOUNDARY INTEGRAL FORMULATION FOR THE PREDICTION OF SOUND RADIATION. Journal of Sound and Vibration, 202(4), 491–509.

[3]El-Samanoudy, R. T. M., & El-Baz, A. M. R. Considerations of Stress Limiter for the SST Turbulence Model in Dual Throat Nozzle Predictions, 2016.

[4] Ewert, Appel, Dierke, Herr "RANS-CAA Based Prediction of NACA 0012 Broadband Trailing Edge Noise and Experimental Validation", 15th AIAACEAS Aeroacoustics Conference (30th AIAA Aeroacoustics Conference), 2009

[5]F.R. Menter, M. Kuntz, and R. Langtry. Ten years of industrial experience with the SST turbulence model. In Proceedings of the fourth international symposium on turbulence, heat and mass transfer, pages 625–632, Antalya, Turkey, 2003. Begell House.

[6]Gee, K. L., Neilsen, T. B., Wall, A. T., Downing, J. M., & James, M. M. (2013). The “sound Of Freedom” Characterizing Jet Noise From High-Performance Military Aircraft. Acoustics Today, 9(3), 8

[7]Huo Y., "Model of F-16 Fighter Aircraft - Equation of Motions", Dept. of electrical Engineering - Systems University of Southern California Los Angeles, CA 90007.

[8]J. E. Ffowcs-Williams and D. L. Hawkings. Sound Generation by Turbulence and Surfaces in Arbitrary Motion. Proc. Roy. Soc. London, A264:321-342, 1969.

[9]K. S. Brentner and F. Farassat. An Analytical Comparison of the Acoustic Analogy and Kirchhoff Formulations for Moving Surfaces. AIAA Journal, 36(8), 1998.

[10]Lockard D.P., "A Comparison of Ffowcs Williams-Hawking;s Solvers for Airframe Noise Applications", 8th AIAA/CEAS Aeroacoustics Conference, June 17-19, 2002.

[11]Lyrintzis, A. S. (2003). Surface Integral Methods in Computational Aeroacoustics—From the (CFD) Near-Field to the (Acoustic) Far-Field. International Journal of Aeroacoustics, 2(2), 95–128.

[12]M. Shur, P. R. Spalart, M. Strelets, A. Travin. Detached-Eddy Simulation of an Airfoil at High Angle of Attack. 1999.

[13]McLaughlin, D. K., Morris, P. J., & Martens, S. (2019). Scaled Demonstration of Fluid Insert Noise Reduction for Tactical Fighter Aircraft Engines. Journal of Aircraft, 1–7.

[14]Menter, F. R. (1993), "Zonal Two Equation k-ω Turbulence Models for Aerodynamic Flows", AIAA Paper 93-2906.

[15]Menter, F. R. (1994), "Two-Equation Eddy-Viscosity Turbulence Models for Engineering Applications", AIAA Journal, vol. 32, no 8. pp. 1598-1605.

[16]Menter, F. R., "Improved Two-Equation k-omega Turbulence Models for Aerodynamic Flows," NASA TM 103975, October 1992

[17]Nitzkorski Z. L.,"A novel porous Ffowcs-Williams and Hawkings acoustic methodology for complex geometries", pp 1-2, 2015

[18]Pääkkönen, R., Kuronen, P., Acta Acustica united with Acustica, Volume 84, Number 1, JanuaryFebruary 1998, pp. 91-96(6)

[19]Sarlak, H., Mikkelsen, R., Sarmast, S., & Sørensen, J. N. (2014). Aerodynamic behaviour of NREL S826 airfoil at Re=100,000. Journal of Physics Conference Series, 524, 012027.

[20]Singer, B. A., Lockard, D. P., & Brentner, K. S. (2000). Computational Aeroacoustic Analysis of Slat Trailing-Edge Flow. AIAA Journal, 38(9), 1558–1564.

[21]Spalart, P. R., Jou, W.-H., Stretlets, M., and Allmaras, S. R. (1997), "Comments on the Feasibility of LES for Wings and on the Hybrid RANS/LES Approach", Advances in DNS/LES, Proceedings of the First AFOSR International Conference on DNS/LES.

[22]Strelets, M. (2001), "Detached Eddy Simulation of Massively Separated Flows", AIAA 2001-0879.

[23]Viswanathan, K., Krothapalli, A., Seiner, J. M., Czech, M. J., Greska, B., & Jansen, B. J. (2011). Assessment of Low-Noise Nozzle Designs for Fighter Aircraft Applications

[24]Von Gierke, H. E. (1953). Physical Characteristics of Aircraft Noise Sources. The Journal of the Acoustical Society of America, 25(3), 367–378.

[25]Wilcox, D. C., "Formulation of the k-omega Turbulence Model Revisited," AIAA Journal, Vol. 46, No. 11, 2008, pp. 2823-2838

[26]Wilcox, D. C., Turbulence Modeling for CFD, 3rd edition, DCW Industries, Inc., La Canada CA, 2006.

[27]Wilcox, D.C. (1988), "Re-assessment of the scale-determining equation for advanced turbulence models", AIAA Journal, vol. 26, no. 11, pp. 1299-1310.